Powder Technology 354 (2019) 158–164

Contents lists available at ScienceDirect

Powder Technology

journal homepage: www.elsevier.com/locate/powtec

Apparent activation energy of multicomponent transition metal oxalates to probe synthesis of battery precursor materials

Hongxu Dong, Eiche Gardner, Alexandra Fay Barron, Gary M. Koenig Jr *

Department of Chemical Engineering, University of Virginia, 102 Engineers Way, Charlottesville, VA USA22904-4741, United States of America

ARTICLE INFO

Article history:
Received 28 March 2019
Received in revised form 23 May 2019
Accepted 31 May 2019
Available online 04 June 2019

Keywords:
Coprecipitation
Crystallization
Activation energy
Lithium-ion battery
Cathode materials

ABSTRACT

In this study the apparent activation energy of pure and multicomponent transition metal oxalate coprecipitation reactions were experimentally measured via time dependent extinction of light passing through the reaction solution. These measurements provide a quantitative descriptor of the influence of the relative transition metal composition on the nucleation and growth processes of the precipitates. The resulting crystal structures of the synthesized precursors were also determined and put into the context of the measured coprecipitation apparent activation energies, revealing that the apparent activation energy may indicate impurity or secondary phase formation before it was detectable with X-ray diffraction. This paper is the first report of using apparent activation energies to investigate battery precursor coprecipitation reactions, and these methods should be extendable to chemistry for coprecipitation of many multicomponent transition metal particles which have applications in multiple fields including energy storage materials.

1. Introduction

Lithium-ion (Li-ion) batteries are a major technology for consumer electronics and one of the few options for energy storage in transportation applications due to the high energy and power densities that can be achieved [1,2]. While many components and physical properties have an important role in the electrochemical charge and discharge processes, the intrinsic properties of the cathode active materials are among the most important that define the limits of the performance metrics of the battery which include electrochemical capacity, rate capability, cycling stability, and cost [3–5]. Extensive research has reported the optimization of cathode active materials through various strategies including metal ion substitution, surface coating, and particle morphology control to improve the electrochemical properties of the resulting batteries [6–12]. While there are many routes to improve cathode material performance and there are many cathode materials to choose from, high levels of control over the composition and phase of the final cathode material are always needed to produce high performance and reproducible battery active materials regardless of the cathode chemistry.

Coprecipitation is a popular method reported in the literature to produce transition metal (TM) precursors which are subsequently lithiated and calcined to produce Li-ion battery active materials [13–20]. The method is straightforward to scale up to larger volume material production and is amenable to both batch and continuous systems [14,21,22]. Even though precipitation synthesis procedures are often straightforward, careful control over the solution chemistry can result in complex compositions and morphologies such as compositional core-shell particles [23–26], particles with gradients from core to surface in their concentration [27–29], and a diversity of shapes including spheres, rods, plates, and dumbbells [11,14,30–32]. While precipitation is a robust and scalable route to synthesize battery active material precursors and complex compositions and morphologies are possible, methods are needed to characterize the precipitation process to improve rational and predictive control of these materials. For example, previous work has demonstrated that in some cases the TM precursors (and subsequently the TM oxide final active materials) had compositions that significantly deviated from feed stoichiometry to the synthesis process, resulting in deleterious effects on the electrochemical performance of the final active material [14,33]. In-situ tracking of the concentrations of the TMs in the solid and liquid phase in the reactor was demonstrated as one method to characterize the precipitation process and understand the origins of compositional deviations [14]. Subsequent follow up reports demonstrated that combining the in-situ concentration information during synthesis with in-situ tracking of the evolution of the particle size distribution yields further insights into the rate of precipitation of the precursors and the different nucleation and growth regimes the particles can experience as a function of TM composition in the feed [34]. These previous reports were focused on compositional deviations of the TM precursors, but producing pure and/or controllable crystal phases of the precursor is also important to synthesizing high performance electrode materials. In particular, phase pure particles are often needed to rationally guide particle morphology [11], and if the particles

* Corresponding author.
E-mail addresses: hd5cw@virginia.edu (H. Dong), epg9ej@virginia.edu (E. Gardner), afb2ex@virginia.edu (A.F. Barron), gary.koenig@virginia.edu (G.M. Koenig).

https://doi.org/10.1016/j.powtec.2019.05.082
0032-5910/

are not phase-pure the appropriate amount of lithium salt to add before calcination can be challenging to determine [29].

In this manuscript, a method will be demonstrated to probe the apparent activation energy during the coprecipitation of TM battery precursors. It is noted here that the activation energies calculated from the experimental method in this study result from a combination of physical and chemical processes including mass transfer, chemical reaction, nucleation formation and initial growth and thus the energies are referred to as apparent activation energies. To our knowledge, this method has never been applied to investigate battery precursor particles, nor to the TM oxalates that will be the focus of this study. The method was based on similar analysis applied to the formation of vanadium oxide precipitates – although in contrast to the present report the vanadium precipitates contained a single TM and were presumably all of the same composition and crystal structure [35]. The precipitation of metal oxalate was chosen as the exemplar system because TM oxalates have previously been reported as precursors for the synthesis of high performance battery materials [14,36,37]. In addition, oxalate forms phase pure dihydrate precursors across a variety of TMs used for Li-ion battery cathodes, including Co, Mn, and Ni. In this study, Mn oxalate, Ni oxalate, and blends of Mn and Ni oxalate of varying Mn:Ni ratios were investigated. Such precursors can be lithiated and calcined to different final active materials depending on their Mn:Ni ratio, for example $LiMn_{0.5}Ni_{0.5}O_2$ for Mn:Ni 1:1 or $LiMn_{1.5}Ni_{0.5}O_4$ for Mn:Ni 3:1 [38,39]. This report will first present the apparent activation energies of Mn and Ni oxalate coprecipitations at different Mn:Ni feed compositions. Then, the sensitivity of the crystal structure of the produced precipitates, determined from refinement of powder X-ray diffraction patterns, to the Mn:Ni composition will be reported in the context of the apparent activation energy results. The results presented suggest that the apparent activation energy reflects the composition-dependent structure of the precipitate particles that form in the reaction solution. It is expected that this analysis would be valuable for any battery precursor system where multiple structural phases are present, which is the case for not only TM oxalate precipitation but also for other TM precursor systems such as TM carbonate and hydroxide [29].

2. Material and methods

2.1. Measurement of coprecipitation induction time

Coprecipitation of TM oxalate particles was conducted by mixing solutions of dissolved TM sulfate with dissolved sodium oxalate. Laboratory grade $MnSO_4 \cdot H_2O$, $NiSO_4 \cdot 6H_2O$, and $Na_2C_2O_4$ (all from Fisher) were used for the coprecipitation reaction. 50 mL of 15 mM TM solution with varying Mn:Ni ratios and 50 mL of 15 mM oxalate solution were prepared separately by dissolving TM salts and oxalate salt. The solutions were heated to the desired target temperature (50, 55, 60, and 65 °C for each Mn:Ni concentration investigated) and then mixed together all at once by pouring the TM solution into the oxalate solution. The mixed solution was homogeneously mixed with a stir bar rotating at 300 rpm for 10 s and then a small portion of the solution was poured into a 3 mL sample cuvette. The cuvette was then quickly put into an ultraviolet-visible (UV-Vis) spectrometer (PerkinElmer Lambda 35) and the transmitted intensity of light at a wavelength of 480 nm that reached the detector after passing through cuvette was collected every 10 s. The experiment was concluded when the measured extinction of transmitted light decreased after reaching a plateau, which occurred after 500 to 1000 s depending on the solution temperature and feed composition. The wavelength of 480 nm was chosen for analysis because at this wavelength solutions of dissolved Ni and Mn salts both had negligible extinction. It was thus assumed that any increases in extinction resulted from light being scattered by the resulting solid particles that nucleate and grow during the coprecipitation process. Throughout the UV–Vis measurements, the cuvette was in a temperature-controlled cuvette holder (PerkinElmer PTP-1 Peltier System) which maintained the solution temperature at the target temperature for the duration of each coprecipitation experiment. The fast transfer of the coprecipitation solution from the heated and temperature-controlled batch reactor to the temperature-controlled cuvette holder was assumed to maintain the solution temperature throughout the duration of the experiment. Although coprecipitation of battery precursors is typically performed with stirring [6–8,11,14–30], the analysis in this study focused on the nucleation and growth processes during coprecipitation in an unmixed cuvette – with the mixing in the batch reactor assumed to provide an initial homogeneous mixing of solution species. Detailed stirring conditions and geometry impact the nucleation and growth and resulting morphology of precursor particles, and because this study focused on the impact of solution composition on nucleation and growth an analysis of different stirring conditions was not conducted.

An example of the measured extinction as a function of reaction time is shown in Fig. 1a. It can be seen that the extinction was low at the beginning of the reaction because the particles that scatter the light have not yet had significant nucleation. As the time elapsed, the extinction slowly increased and then transitioned to a region where it increased linearly with time. After this linear increase the extinction would reach a maximum and then slowly start to decrease. The general profile of the extinction as a function of time was the same for all TM ratios synthesized, and thus the process was considered in the context of three different regions separated by dashed lines in Fig. 1a. Region I was the inert period when the reactant species have mixed but particle nucleation has not reached a significant extent and thus the curve was almost horizontal. Region II was the transition period when the nuclei have stabilized and started

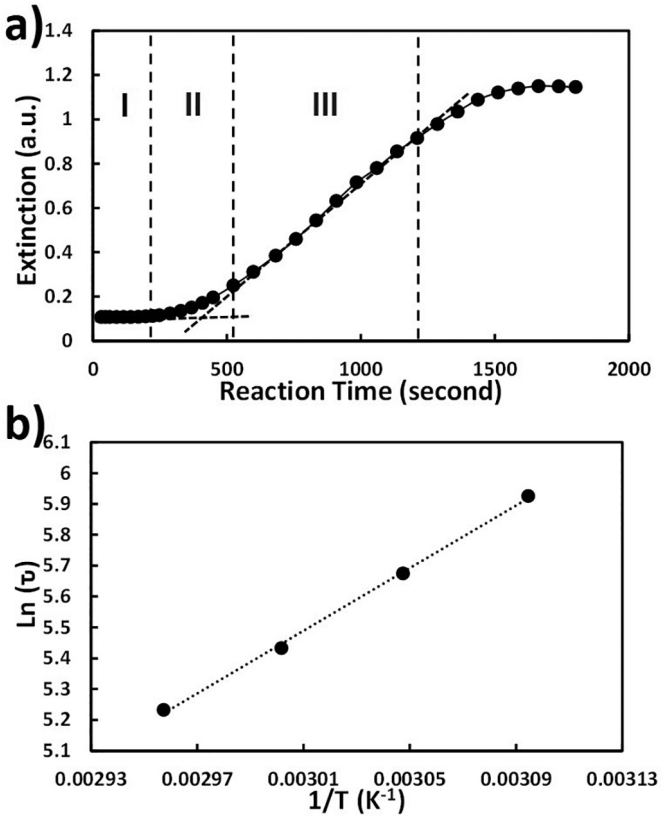

Fig. 1. a) Extinction at 480 nm measured using UV-Vis on the coprecipitation reaction solution as a function of time. Regions I, II, and III are discussed in the text and the general profile was representative for all solution compositions investigated. b) Example of plot used to extract the apparent activation energy from the induction time measured as a function of temperature assuming Arrhenius behavior. For both a) and b) all precipitations were conducted with 15 mM total TM in the initial solution and a 3:1 Mn:Ni ratio. The temperature for a) was 50 °C.

to grow. Region III was the period of continuous and fast particle growth. Both region I and region III of the curve were linear and were fit using least squares methods, and dashed lines of best fit have been added in Fig. 1a. The coprecipitation particle growth starting point, or induction time (τ) was determined by the intersection between the lines of best fit for the inert region (I) and the growth region (III). This method for measuring τ was both a reliable and reproducible way to measure the induction period as opposed to visual observation of the reaction solution [35]. Experiments measuring τ were conducted at multiple temperatures and multiple Mn:Ni ratios, and each specific temperature and solution composition was repeated at a minimum in triplicate to determine average induction times. As will be described below, these induction times were used to calculate apparent activation energies.

2.2. Calculation of apparent activation energy

To determine the apparent activation energy, the induction time was assumed to follow Arrhenius behavior. For each TM solution ratio, the average induction time was measured at four different temperatures. Fig. 1b shows an example of how the induction time information was then used, where plots were generated with $\ln(\tau)$ on the y-axis and the inverse of the reaction temperature (in °K) on the x-axis. Assuming Arrhenius behavior for the induction process, the relationship between induction time and temperature would be of the form [40]:

$$\ln(\tau) = -\ln(A) + \frac{E}{k_B T} \quad (1)$$

where A is the pre-exponential constant, E is the apparent activation energy and k_B is Boltzmann's constant. The slope of a linear fit of $\ln(\tau)$ versus 1/T thus yields E/k_B and a value for E, the apparent activation energy for those solution conditions. Thus, the slope of the line of best fit in Fig. 1b is equal to E/k_B and the apparent activation energy can be determined from this analysis.

2.3. Materials characterization

For material characterization, larger scale synthesis was conducted for each Mn:Ni ratio and the precursor particles were filtered, rinsed with distilled water, and put into an oven (Carbolite) at 80 °C in an air atmosphere overnight to dry the powder. More detailed description of the synthesis process can be found in previous publications [14,41]. The process and reaction conditions were all the same as used for the induction time measurements except that the total solution volume was increased to 800 mL and the synthesis was conducted within a 1 L beaker. The crystal structures of the resulting coprecipitated particles were analyzed by powder X-ray diffraction (XRD) with a PANalytical X'pert ProMPD using a Cu-Kα radiation source. Fullprof was used to find the lattice parameters of each sample [42]. Thermal gravimetrical analysis (TGA, TA Q50) was conducted to measure the temperatures of structural water loss and oxalate decomposition, which were each determined by peaks in the plot of the differential mass change as a function of temperature. All TGA measurements were performed in air with a heating rate of 10 °C min^{-1}. Scanning electron microscopy (SEM, FEI Quanta 650) was conducted on particles after complete drying to a powder and then mounting on SEM stubs.

3. Results and discussion

It was postulated that apparent activation energy of the nucleation and growth of the coprecipitated particles would provide a quantitative route to understand the impact of solution composition on the phase of the resulting particles which form. This idea was based on previous observations that at the solution conditions used in this study 1) pure Mn and Ni oxalate form different phases, and 2) pure Mn and Ni oxalate precipitate at very different rates [14]. Thus, it was expected that apparent activation energy would provide a quantitative descriptor that differentiates Ni from Mn precipitation. Given that the pure Mn and Ni oxalates form different phases, it was expected that they would have limits to the extent to which they could form a solid solution, and thus the apparent activation energy might also provide insights into the solution conditions where a second phase started to precipitate. It was expected that Arrhenius behavior for the coprecipitation reaction would be appropriate, as it had been previously applied to other crystallization processes [35,43]. Initial experiments such as those in Fig. 1b also revealed good linear relationships when using the linearized form of the Arrhenius relationship with respect to τ (Eq. 1), and as will be described in further detail across all reaction conditions the fit was very good.

The apparent activation energies determined for each solution composition are shown in Fig. 2. Error bars represent the standard deviation between the experimental data and the least squares fit to determine the activation energy, and some were quite wide. Large error bars may have been due to a number of factors, including local temperature fluctuations during coprecipitation, surface imperfections of the vial containers, or inhomogeneity in the local mixing provided by the stirring [44–46]. In addition, crystallization is inherently a stochastic process, and in the relatively low concentration regime where this study was conducted fluctuations in the timescale for stable nuclei to form would be expected to decrease the measurement precision. Under synthesis conditions where more than one type of nuclei may form, the stochastic distribution of those nuclei would also increase the measurement error. Finally, crystallization can be very sensitive to seeding, and thus solid particles/dust in the reaction solution or on the cuvette surface could impact the nucleation and growth timescale. While some of the processes described above would be difficult to remove from the system (e.g., stochastic crystallization process and formation of different nuclei types) improvements in conditions such as surrounding particulate concentration in the air may help improve the measurement precision. The detailed numerical values associated with these energies can be found in Supplementary Information, Table S1. The R^2 values were almost all larger than 0.9, indicating a good linear fit of Eq. 1 across the range of Mn feed compositions explored. The smallest R^2 value is 0.85 at Mn feed content of 70% while values of other feed compositions were all above 0.9 (Table S1).

To facilitate discussion of results, the nomenclature MnXXNiYY will be used, where the "XX" and "YY" represent the feed solution to the reaction being XX mol% Mn and YY mol% Ni. Mn100 and Ni100 represent the pure Mn and pure Ni coprecipitation. The activation energies of pure Mn and pure Ni oxalate coprecipitation were determined to be 37.8 ± 13.2 kJ mol^{-1} and 21.4 ± 9.46 kJ mol^{-1}, respectively. These quantitative results, with Mn oxalate having a lower apparent activation energy for coprecipitation, were in agreement with observations that Mn oxalate

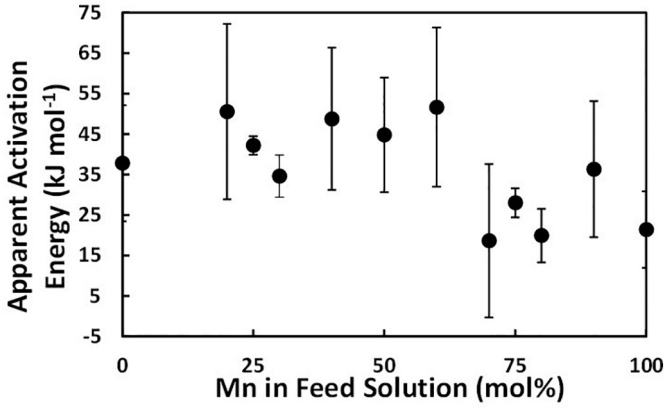

Fig. 2. Apparent activation energies of the coprecipitation reactions with differing feed Mn:Ni ratios. Error bars represent the standard deviation between the experimental data and the least squares fit to determine the activation energy.

coprecipitated faster than Ni oxalate under otherwise identical reaction conditions.

Comparing the activation energies of coprecipitations with Mn feed molar percentage between 20% and 50% (Fig. 2), there was a slight trend of increasing activation energy with increasing Mn in the feed solution, though the size of the error bars makes concrete assignment of this effect challenging. It is noted that within this range as the Mn feed content increased the intercept of the Arrhenius fits decreased (data not shown). The decrease in the intercept reflected a decrease in the pre-exponential term of the Arrhenius equation (Eq. 1). The decrease of the pre-exponential constant with increasing relative Mn in the coprecipitation solution reflected a decrease in the absolute crystallization rates. This analysis was consistent with the decrease of the induction times across all temperatures that the coprecipitation was performed (Fig. 3). It can be seen in Fig. 3 that there was a significant drop of induction times from pure Ni coprecipitation to 20 mol% Mn blend coprecipitation and then a slow decrease of the induction time as the Mn content was further increased until 70 mol% Mn was used. A slight local minimum in the induction time measured at all temperatures at 20 mol% Mn may have been due to transformation of the crystallization mechanism from homogeneous to heterogeneous crystallization [44], due to a seeding effect that the initial and fast forming manganese oxalate nuclei acting as the seeds to facilitate faster nickel precipitation [14]. This seeding effect and subsequent observation of qualitative reduction in induction time was previously suggested and supported by experimental evidence via pure Mn oxalate seed addition at the initiation of pure Ni oxalate coprecipitation in a previous study [14,47]. The slight increase of the apparent activation energy with increasing Mn content in the feeding solutions, while in contrast to the absolute induction time measurements, may indicate structural distortion of the precipitate particles as they start to grow due to the different phases of the initial nuclei seeds and the later larger crystals that form (crystal structure discussed in further detail below) [41]. The high Mn content seeds may result in a higher barrier for Ni precipitation which would be reflected by the increasing activation energy, while the apparent crystallization rates represented via induction time were decreased due to the compensation by the increase of fast-forming Mn nuclei which provided more seed surface to facilitate a higher overall precipitation rate.

Inspection of Fig. 2 reveals a significant drop of apparent activation energy when the Mn content increased to 70% of the feed solution. The activation energy at 70 mol% Mn was calculated to be 18.7 ± 18.9 kJ mol^{-1}, significantly smaller compared to the 37.8 ± 13.2 kJ mol^{-1}, 42.2 ± 2.29 kJ mol^{-1}, and 44.8 ± 14.1 kJ mol^{-1} of Ni100, Mn25Ni75 and Mn50Ni50 coprecipitations. It is speculated that this decrease in the apparent activation energy may have reflected a phase transition in the formed Mn Ni oxalate particles. As shown in the XRD patterns of the obtained Mn Ni oxalate particles (Fig. 4a), the particles collected from feed solutions with 90 mol% or higher Mn content in the feed solution exhibited the peaks of Mn oxalate, while the particles collected from feed solutions with less than 90 mol% Mn had peaks consistent with the structure of Ni oxalate. Previous literature has reported that the orthorhombic β-$MC_2O_4 \cdot 2H2O$ (where M stands for the d-block TM) with space group $P2_12_12_1$ was a thermodynamically preferred and more stable structure compared to the α-$MC_2O_4 \cdot 2H2O$ with monoclinic space group C2/c [48–50]. In the coprecipitation conditions in this paper, pure Ni oxalate formed the β phase and pure Mn oxalate formed the α phase. The Ni oxalate β phase being the dominant structure across most of the

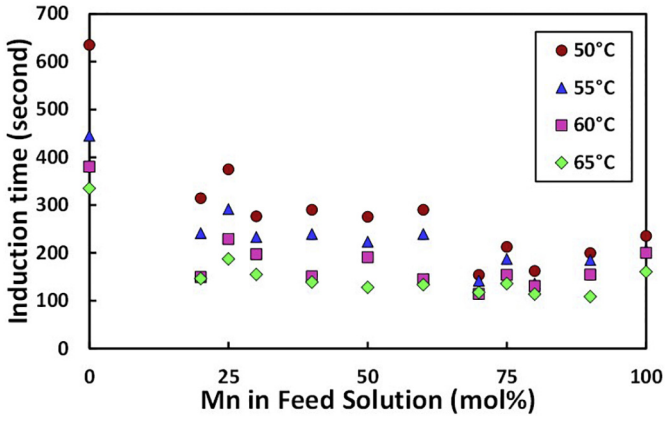

Fig. 3. Measured induction times of the coprecipitation reactions with different feed Mn:Ni ratios at 50 °C (red circles), 55 °C (blue triangles), 60 °C (pink squares), and 65 °C (green diamonds). (For interpretation of the references to colour in this figure legend, the reader is referred to the web version of this article.)

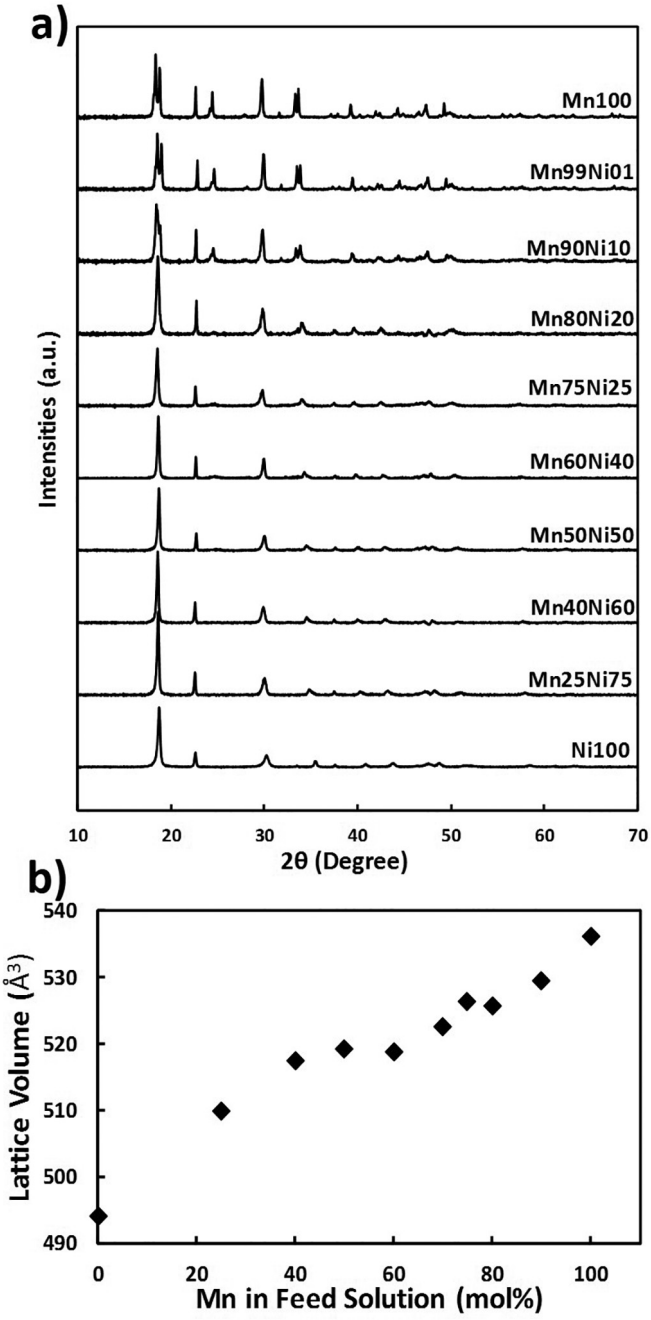

Fig. 4. a) XRD patterns of the obtained precipitate particles with varying Mn:Ni ratio feed concentrations. MnXXNiYY indicates the feed was XX mol% Mn and YY mol% Ni. b) Lattice volumes determined from refining the patterns in a).

Table 1
Lattice parameters determined from Rietveld refinement of the XRD patterns for oxalate precipitates formed with different Mn:Ni ratios in the feed. The differential mass loss peak temperatures from TGA analysis associated with structural water loss and oxalate decomposition are also listed for each feed condition.

Mn in the Feed Solution (mol %)	Phase	Lattice Parameters				Lattice Volume (Å^3)	Peak in Differential Mass Loss (°C)	
		a	b	c	β		Structural Water Loss	Oxalate Decomposition
0	β	11.81	5.33	15.70		494.1	193	316
25	β	11.91	5.44	15.74		509.9	187	304
40	β	11.97	5.49	15.75		517.5	173	299
50	β	11.97	5.52	15.72		519.3	191	298
60	β	11.98	5.52	15.69		518.8	189	290
70	β	12.01	5.55	15.68		522.6	181	283
75	β	12.00	5.57	15.75		526.4	175	280
80	β	12.00	5.58	15.69		525.7	162	284
90	α	12.00	5.63	10.00	128.4	529.6	158	278
100	α	12.08	5.66	10.03	128.6	536.2	117	272

compositional range (until 90 mol% Mn) was consistent with the higher stability of the β phase dictating the crystal structure of the resulting oxalate material powder. Also, the substitution of Mn would be expected to distort the crystal structure, which may have resulted in a slight increase in the apparent activation energy as a function of Mn mol% in the feed as the Mn was increased from 0 to 60 mol% (although it is noted the standard deviation in the apparent activation energy measurements was relatively high). The decrease of the activation energy at Mn70Ni30 composition may have been due to a phase transition of the bulk precipitates formed early in the coprecipitation from orthorhombic β-phase to the monoclinic α-phase, which is the phase of Mn concentrated seeds. The structural similarity between the early formed Mn oxalate seeds and the particles subsequently growing on these seeds would have reduced the apparent activation barrier of the particle nucleation and growth [44]. Previous studies on calcium carbonate coprecipitation reactions have revealed that higher similarity between the precipitates and the seeds resulted in a significant increase in reaction rates [51,52]. Although the apparent activation energy measurements suggested that the precipitate particles formed may have been α phase at a feed of 70 mol% Mn, the α phase was not observed in powder XRD until the Mn in the feed was 90 mol%. The higher Mn composition required to observe the α phase in XRD may be due to the fact that the phase transition only happened locally and on the early formed precipitates and that gradually the more stable β phase was the dominant crystal structure that grew during the coprecipitation. If the amount of a phase was relatively small relative to the total sample mass, as well as buried within the cores of the precipitate particles, it would not be expected to be detected with powder XRD. The calculated lattice parameters and lattice volumes of the oxalate powders were obtained using Rietveld refinement and are summarized in Table 1. The lattice volumes as a function of Mn content in the solution are also plotted in Fig. 4b. It can be seen that the lattice volume increased as the Mn content increased, consistent with Mn^{2+} having a larger ionic radius than Ni^{2+} [14].

As the manganese content was increased to 100% in the solution (pure Mn coprecipitation), the activation energy was 21.42 ± 9.46 kJ mol^{-1}, similar to that of the phase transition point. It can be seen from the plot that in each of the two single-phase ranges of the precipitation reaction, there appeared to be a peak of the activation energy in the middle of the composition range while the activation energy was the lowest for the pure feed solution. This may reflect the distorted structure of the precipitate due to the existence of multiple TM ions with different sizes in the structure.

TGA analysis was also conducted with the collected precipitate particles. All materials had two distinct peaks in differential mass loss. The first reflected the loss of structural water, which typically occurred at below 200 °C and has previously been used to indicate the structural stability of a material [41,53]. Higher structural water loss temperature implies a more stable structure which holds the structural water more tightly. The differential mass loss peak associated with structural water loss as a function of Mn mol% in the feed solution is shown in Fig. 5, with numerical values provided in Table 1. It can be seen that the temperature of structural water loss increased with increasing Ni content (or decreasing Mn content) in the solution, and concurrently incorporated into the precipitate phase. This observation was in agreement with the higher stability of the β phase which pure Ni oxalate formed [14]. As Mn content was increased in the feed solution and in the precipitate structure, the formed precipitate underwent constantly increasing structural distortion in the single β phase as Mn content increased, reducing the structural stability of the phase and decreasing the structural water loss temperature. When Mn content reached the threshold of phase transition to the Mn oxalate phase which formed the less stable α phase, the drop of structural stability would be expected to accelerate the decrease in the structural water loss temperature. This expectation was consistent with the significant decrease in the structural water loss temperature when 70 mol% Mn was in the feed (Fig. 5). The increasing sensitivity to the Mn content on the structural water loss occured at the composition where apparent activation energy had a dramatic change, indicating that the change in phase of the precipitates may impact the structural stability of the material even as the bulk phase observed in XRD does not have a detectable phase transition. The peak temperature in differential mass loss for oxalate decomposition as a function of Mn content in the feed solution was also plotted in Fig. 5 (numerical values in Table 1). The oxalate decomposition temperature also decreased as more Mn was added to the particles, although the decrease appeared to have a similar gradual slope across the compositional range.

Fig. 6 contains SEMs showing the morphology of particles collected after coprecipitation under different solution compositions. The Ni100 particles (Fig. 6a) were relatively small and have smooth surfaces, consistent with the slower precipitation for Ni oxalate and the formation of

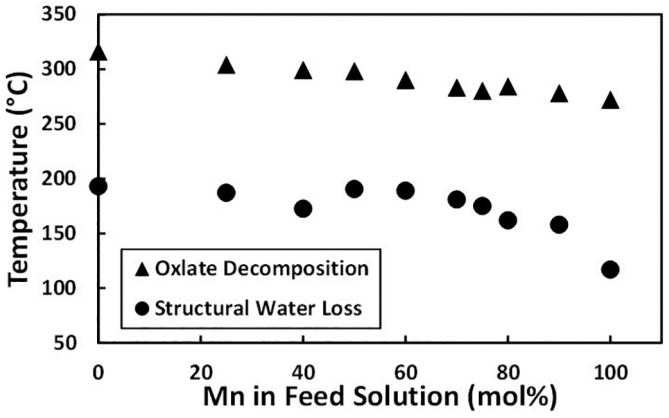

Fig. 5. Peaks in differential mass loss from TGA on the powders collected from the different reaction solutions corresponding to oxalate decomposition (black triangles) and structural water loss (black circles).

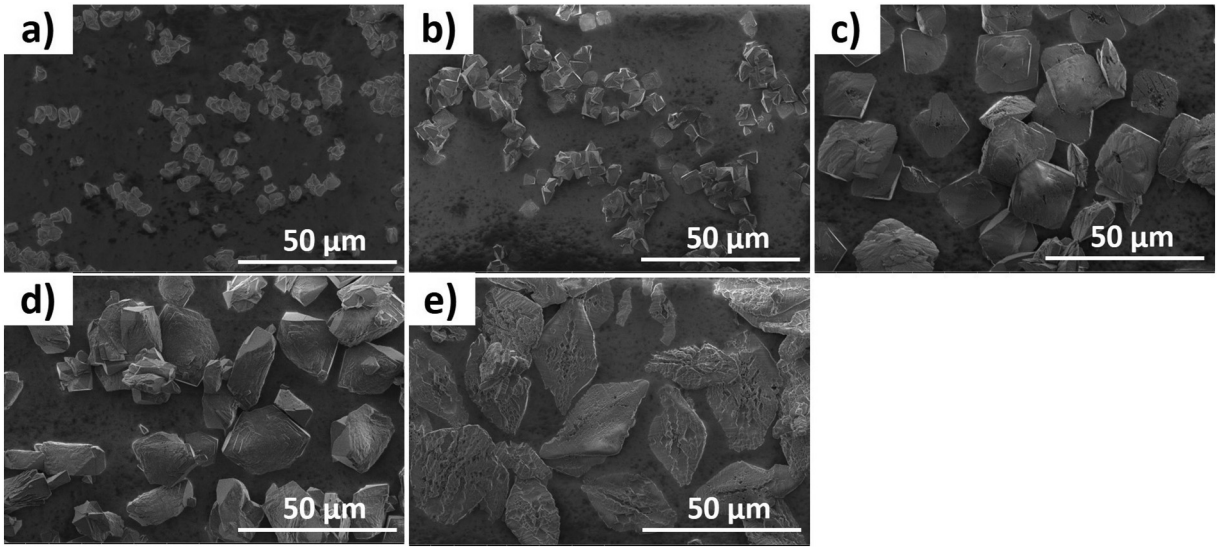

Fig. 6. SEM images of oxalate particles collected from the feed coprecipitation solutions of a) Ni100, b) Mn10Ni90, c) Mn50Ni50, d) Mn75Ni25, and e) Mn100. MnXXNiYY indicates the feed was XX mol% Mn and YY mol% Ni.

new nuclei throughout the coprecipitation process for these materials [34]. The Mn10Ni90 particles (Fig. 6b) had very similar morphology to the Ni100 particles, suggesting a similar process for nucleation and growth. This would suggest the formation of similar seed nuclei to those of Ni oxalate, although the increased Mn composition would be expected to impact the strain in the resulting particles that formed. The Mn50Ni50 particles (Fig. 6c) were larger than the higher Ni composition particles, however, the surface was still relatively smooth and the geometry of the particles appeared close to quadrilateral. The Mn75Ni25 (Fig. 6d) and Mn100 (Fig. 6e) were similar in terms of size and shape, although the Mn100 particles were larger and had noticeably rougher surfaces. The morphology of the Mn75Ni25 and Mn100 particles suggested a fundamentally different nucleation and growth process relative to the high Ni composition particles (Ni100 and Mn10Ni90). These morphologies and their corresponding changes in nucleation and growth processes were consistent with the differences observed in apparent activation energy.

The results presented above, when combined, suggest that the apparent activation energies for the precipitates with varying compositions of the blend of TMs provide insights into the composition where precipitate particles of different phases start to form. While after full growth of the particles the new phase does not always have the necessary amount and/or crystallinity of material to be detected in powder XRD analysis, the local minimum of the activation energy can be used to determine the solution conditions where multiple phases of nuclei may form in the solution. It should be noted that it is suspected that the local minimum in apparent activation energy resulted from the new phase facilitating the growth stage of the precipitation by seeding further growth faster due to the similarity between seeds and the phase of the particles that continued to grow. Thus, other systems may behave quite differently depending on whether there are two polymorphs dependent on the TM or cations used, and the relative stability and apparent activation energy of the pure phase materials. Further study will also be needed to confirm the speculation on the formation of both phases during the nucleation phase of the precipitation.

4. Conclusions

This report probed the interactions within a multicomponent cation coprecipitation process via apparent activation energy measurements for particles often used as precursors to synthesize battery materials. Apparent activation energy was measured by analysis of induction times of the crystallization reaction process as a function of temperature using UV–Vis spectroscopy. It was found that a local minimum of the experimentally measured activation energy occurred near the composition where a new phase becomes preferred for the resulting precipitate particles. The observed minimum in the apparent activation energy appeared to be consistent with where the precipitate particles of different phases formed, although one of the phases was not detected in the final particles using bulk XRD on the collected particles, suggesting they were not retained in sufficient amount and/or crystallinity during the more substantive growth phase of the material. The apparent activation energy analysis is expected to provide valuable insights to many coprecipitation processes with multicomponent cations where multiple phases may have been observed depending on solution conditions.

Acknowledgments

This work was supported by the National Science Foundation, through grant awards CBET-1652488 and ECCS-1405134. The authors also thank Prof. Geoff Geise for use of their lab's TGA instrument.

Appendix A. Supplementary data

Supplementary data to this article can be found online at https://doi.org/10.1016/j.powtec.2019.05.082.

References

[1] J.B. Goodenough, Y. Kim, Challenges for rechargeable Li batteries, Chem. Mater. 22 (2010) 587–603, https://doi.org/10.1021/cm901452z.
[2] J.B. Goodenough, K.-S.S. Park, The Li-ion rechargeable battery: a perspective, J. Am. Chem. Soc. 135 (2013) 1167–1176, https://doi.org/10.1021/ja3091438.
[3] B. Scrosati, J. Garche, Lithium batteries: status, prospects and future, J. Power Sources 195 (2010) 2419–2430, https://doi.org/10.1016/j.jpowsour.2009.11.048.
[4] C.M. Julien, A. Mauger, Review of 5-V electrodes for Li-ion batteries: status and trends, Ionics (Kiel) 19 (2013) 951–988, https://doi.org/10.1007/s11581-013-0913-2.
[5] D.L. Wood, J. Li, C. Daniel, Prospects for reducing the processing cost of lithium ion batteries, J. Power Sources 275 (2015) 234–242, https://doi.org/10.1016/j.jpowsour.2014.11.019.
[6] T.H.H. Cho, S.M.M. Park, M. Yoshio, T. Hirai, Y. Hideshima, Effect of synthesis condition on the structural and electrochemical properties of Li[Ni1/3Mn1/3Co1/3]O2prepared by carbonate co-precipitation method, J. Power Sources 142 (2005) 306–312, https://doi.org/10.1016/j.jpowsour.2004.10.016.
[7] Y.K. Sun, B.R. Lee, H.J. Noh, H. Wu, S.T. Myung, K. Amine, A novel concentration-gradient Li[Ni0.83Co0.07Mn0.10]O2cathode material for high-energy lithium-ion batteries, J. Mater. Chem. 21 (2011) 10108–10112, https://doi.org/10.1039/c0jm04242k.

[8] L. Li, S. Song, X. Zhang, R. Chen, J. Lu, F. Wu, K. Amine, Ultrasonic-assisted co-precipitation to synthesize lithium-rich cathode Li1.3Ni0.21Mn0.64O2+d materials for lithium-ion batteries, J. Power Sources 272 (2014) 922–928, https://doi.org/10.1016/j.jpowsour.2014.08.063.
[9] Q. Ma, D. Mu, Y. Liu, S. Yin, C. Dai, Enhancing coulombic efficiency and rate capability of high capacity lithium excess layered oxide cathode material by electrocatalysis of nanogold, RSC Adv. 6 (2016) 20374–20380, https://doi.org/10.1039/C5RA26667J.
[10] F. Wu, H. Lu, Y. Su, N. Li, L. Bao, S. Chen, Preparation and electrochemical performance of Li-rich layered cathode material, Li[Ni0.2Li0.2Mn0.6]O2, for lithium-ion batteries, J. Appl. Electrochem. 40 (2010) 783–789, https://doi.org/10.1007/s10800-009-0057-2.
[11] J.P. Robinson, G.M. Koenig, Tuning solution chemistry for morphology control of lithium-ion battery precursor particles, Powder Technol. 284 (2015) 225–230, https://doi.org/10.1016/j.powtec.2015.06.070.
[12] G.M. Koenig, J. Ma, B. Key, J. Fink, K.-B. Low, R. Shahbazian-Yassar, I. Belharouak, Composite of LiFePO4 with titanium phosphate phases as Lithium-ion battery electrode material, J. Phys. Chem. C 117 (2013) 21132–21138, https://doi.org/10.1021/jp4074174.
[13] H.S. Shin, S.H. Park, Y.C. Bae, Y.K. Sun, Synthesis of Li[Ni0.475Co0.05Mn0.475]O2cathode materials via a carbonate process, Solid State Ionics 176 (2005) 2577–2581, https://doi.org/10.1016/j.ssi.2005.07.008.
[14] H. Dong, G.M. Koenig Jr, Compositional control of precipitate precursors for lithium-ion battery active materials: role of solution equilibrium and precipitation rate, J. Mater. Chem. A 5 (2017) 13785–13798, https://doi.org/10.1039/C7TA03653A.
[15] A. Van Bommel, J.R. Dahn, Analysis of the growth mechanism of Coprecipitated spherical and dense nickel , manganese , and cobalt -containing hydroxides in the presence of aqueous Ammonia, Chem. Mater. 21 (2009) 1500–1503, https://doi.org/10.1021/cm803144d.
[16] G.-H. Kim, S.-T. Myung, H.J. Bang, J. Prakash, Y.-K. Sun, Synthesis and electrochemical properties of Li[Ni[sub 1/3]co[sub 1/3]Mn[sub (1/3−x)]mg[sub x]]O[sub 2−y]F[sub y] via coprecipitation, Electrochem. Solid-State Lett. 7 (2004) A477, https://doi.org/10.1149/1.1809554.
[17] D. Liu, J. Han, J.B. Goodenough, Structure, morphology, and cathode performance of Li1-x[Ni0.5Mn1.5]O4 prepared by coprecipitation with oxalic acid, J. Power Sources 195 (2010) 2918–2923, https://doi.org/10.1016/j.jpowsour.2009.11.024.
[18] X. Lu, C. Liu, W. Zhu, Z. Lu, W. Li, Y. Yang, G. Yang, Synthesis of micron-sized LiNi0.5Mn1.5O4 single crystals through in situ microemulsion/coprecipitation and characterization of their electrochemical capabilities, Powder Technol. 343 (2019) 445–453, https://doi.org/10.1016/J.POWTEC.2018.11.038.
[19] J.H. Kim, W.C. Choi, H.Y. Kim, Y. Kang, Y.-K. Park, Preparation of mono-dispersed mixed metal oxide micro hollow spheres by homogeneous precipitation in a micro precipitator, Powder Technol. 153 (2005) 166–175, https://doi.org/10.1016/J.POWTEC.2005.03.004.
[20] L. Li, X. Li, Z. Wang, H. Guo, P. Yue, W. Chen, L. Wu, A simple and effective method to synthesize layered LiNi0.8Co0.1Mn0.1O2 cathode materials for lithium ion battery, Powder Technol. 206 (2011) 353–357, https://doi.org/10.1016/J.POWTEC.2010.09.010.
[21] D. Wang, I. Belharouak, G.M. Koenig, G. Zhou, K. Amine, Growth mechanism of Ni0.3Mn0.7CO3 precursor for high capacity Li-ion battery cathodes, J. Mater. Chem. 21 (2011) 9290, https://doi.org/10.1039/c1jm11077b.
[22] Y. Kim, D. Kim, Synthesis of high-density nickel cobalt aluminum hydroxide by continuous coprecipitation method, ACS Appl. Mater. Interfaces 4 (2012) 586–589, https://doi.org/10.1021/am201585z.
[23] Y.K. Sun, S.T. Myung, M.H. Kim, J. Prakash, K. Amine, Synthesis and characterization of Li[(Ni0.8Co 0.1Mn0.1)0.8(Ni0.5Mn 0.5)0.2]O2 with the microscale core-shell structure as the positive electrode material for lithium batteries, J. Am. Chem. Soc. 127 (2005) 13411–13418, https://doi.org/10.1021/ja053675g.
[24] Y.K. Sun, S.T. Myung, B.C. Park, K. Amine, Synthesis of spherical nano- to microscale core−shell particles Li[(Ni0.8Co0.1Mn0.1)1-x(Ni0.5Mn0.5)x]O2 and their applications to lithium batteries, Chem. Mater. 18 (2006) 5159–5163, https://doi.org/10.1021/cm061746k.
[25] K.-S. Lee, S.-T. Myung, Y.-K. Sun, Synthesis and electrochemical performances of core-shell structured Li[(Ni1/3Co1/3Mn1/3)0.8(Ni1/2Mn1/2)0.2]O2 cathode material for lithium ion batteries, J. Power Sources 195 (2010) 6043–6048, https://doi.org/10.1016/J.JPOWSOUR.2010.02.002.
[26] Y. Sun, S. Myung, H. Shin, Y.C. Bae, Novel core−shell-structured Li[(Ni0.8Co0.2)0.8(Ni0.5Mn0.5)0.2]O2 via coprecipitation as positive electrode material for lithium secondary batteries, J. Phys. Chem. B 110 (2006) 6810–6815, https://doi.org/10.1021/jp0571473.
[27] Y.-K. Sun, Z. Chen, H.-J. Noh, D.-J. Lee, H.-G. Jung, Y. Ren, S. Wang, C.S. Yoon, S.-T. Myung, K. Amine, Nanostructured high-energy cathode materials for advanced lithium batteries, Nat. Mater. 11 (2012) 942–947, https://doi.org/10.1038/nmat3435.
[28] Y.K. Sun, D.H. Kim, C.S. Yoon, S.T. Myung, J. Prakash, K. Amine, A novel cathode material with a concentration-gradient for high-energy and safe Lithium-ion batteries, Adv. Funct. Mater. 20 (2010) 485–491, https://doi.org/10.1002/adfm.200901730.
[29] G.M. Koenig, I. Belharouak, H. Deng, Y.-K. Sun, K. Amine, Composition-tailored synthesis of gradient transition metal precursor particles for lithium-ion battery cathode materials, Chem. Mater. 23 (2011) 1954–1963, https://doi.org/10.1021/cm200058c.
[30] D.K. Kim, P. Muralidharan, H.-W. Lee, R. Ruffo, Y. Yang, C.K. Chan, H. Peng, R.A. Huggins, Y. Cui, Spinel LiMn2O4 nanorods as Lithium ion battery cathodes, Nano Lett. 8 (2008) 3948–3952, https://doi.org/10.1021/nl8024328.
[31] R. Mei, X. Song, Y. Yang, Z. An, J. Zhang, Plate-like LiFePO4crystallite with preferential growth of (010) lattice plane for high performance Li-ion batteries, RSC Adv. 4 (2014) 5746–5752, https://doi.org/10.1039/c3ra45755a.
[32] G. Li, L. Qi, P. Xiao, Y. Yu, X. Chen, W. Yang, Effect of precursor structures on the electrochemical performance of Ni-rich LiNi0.88Co0.12O2 cathode materials, Electrochim. Acta 270 (2018) 319–329, https://doi.org/10.1016/J.ELECTACTA.2018.03.106.
[33] M.M. Thackeray, Lithiated oxides for Lithium ion batteries, J. Electrochem. Soc. 142 (1995) 2558–2563, https://doi.org/10.1149/1.2050053.
[34] H. Dong, A. Wang, G. Smart, D. Johnson, G.M. Koenig, In-situ analysis of nucleation and growth of transition metal oxalate battery precursor particles via time evolution of solution composition and particle size distribution, Colloids Surf. A Physicochem. Eng. Asp. 558 (2018) 8–15, https://doi.org/10.1016/J.COLSURFA.2018.08.047.
[35] D. Oboroceanu, N. Quill, C. Lenihan, D.N. Eidhin, S.P. Albu, R.P. Lynch, D.N. Buckley, Effects of temperature and composition on catholyte stability in vanadium flow batteries: measurement and modeling, J. Electrochem. Soc. 164 (2017) A2101–A2109, https://doi.org/10.1149/2.1401709jes.
[36] D. Wang, I. Belharouak, G. Zhou, K. Amine, Synthesis of Lithium and manganese-rich cathode materials via an oxalate co-precipitation method, J. Electrochem. Soc. 160 (2013) A3108–A3112, https://doi.org/10.1149/2.016305jes.
[37] Z. Qi, G.M. Koenig, High-performance LiCoO2 sub-micrometer materials from scalable microparticle template processing, Chem. Select 1 (2016) 3992–3999, https://doi.org/10.1002/slct.201600872.
[38] B.L. Cushing, J.B. Goodenough, Influence of carbon coating on the performance of a LiMn0.5Ni0.5O2 cathode, Solid State Sci. 4 (2002) 1487–1493, https://doi.org/10.1016/S1293-2558(02)00044-4.
[39] K. Amine, H. Tukamoto, H. Yasuda, Y. Fujita, Preparation and electrochemical investigation of LiMn2 − xMexO4 (Me: Ni, Fe, and x = 0.5, 1) cathode materials for secondary lithium batteries, J. Power Sources 68 (1997) 604–608, https://doi.org/10.1016/S0378-7753(96)02590-6.
[40] S. Arrhenius, Über die Dissociationswärme und den Einfluss der Temperatur auf den Dissociationsgrad der Elektrolyte, Zeitschrift Für Phys. Chemie. 4U (2017) 96–116.
[41] H. Dong, A. Wang, G.M. Koenig, Role of coprecipitation and calcination of precursors on phase homogeneity and electrochemical properties of battery active materials, Powder Technol. 335 (2018) 137–146, https://doi.org/10.1016/j.powtec.2018.05.020.
[42] J. Rodríguez-Carvajal, Recent advances in magnetic structure determination by neutron powder diffraction, Phys. B Condens. Matter 192 (1993) 55–69, https://doi.org/10.1016/0921-4526(93)90108-I.
[43] D. Oboroceanu, N. Quill, C. Lenihan, D.N. Eidhin, S.P. Albu, R.P. Lynch, D.N. Buckley, Communication—observation of Arrhenius behavior of catholyte stability in vanadium flow batteries, J. Electrochem. Soc. 163 (2016) A2919–A2921, https://doi.org/10.1149/2.0361614jes.
[44] S.K. Myasnikov, A.P. Chipryakova, N.N. Kulov, Kinetics, energy characteristics, and intensification of crystallization processes in chemical precipitation of hardness ions, Theor. Found. Chem. Eng. 47 (2013) 505–523, https://doi.org/10.1134/S0040579513050229.
[45] N. Doki, H. Seki, K. Takano, H. Asatani, M. Yokota, N. Kubota, Process control of seeded batch cooling crystallization of the metastable α-form glycine using an in-situ ATR-FTIR spectrometer and an in-situ FBRM particle counter, Cryst. Growth Des. 4 (2004) 949–953, https://doi.org/10.1021/cg030070s.
[46] R. Doremus, Precipitation kinetics of ionic salts from solution, J. Phys. Chem. (1968) 2158, https://doi.org/10.1021/j150567a011.
[47] M.Z. Mubarok, J. Lieberto, Precipitation of nickel hydroxide from simulated and atmospheric-leach solution of nickel laterite ore, Procedia Earth Planet. Sci. 6 (2013) 457–464, https://doi.org/10.1002/eej.4390960608.
[48] M.C. López, J.L. Tirado, C. Pérez Vicente, Structural and comparative electrochemical study of M(II) oxalates, M = Mn, Fe, Co, Ni, Cu, Zn, J. Power Sources 227 (2013) 65–71, https://doi.org/10.1016/j.jpowsour.2012.08.100.
[49] S. Guillemet-Fritsch, M. Aoun-Habbache, J. Sarrias, A. Rousset, N. Jongen, M. Donnet, P. Bowen, J. Lemaître, High-quality nickel manganese oxalate powders synthesized in a new segmented flow tubular reactor, Solid State Ionics 171 (2004) 135–140, https://doi.org/10.1016/S0167-2738(03)00282-0.
[50] N. Mancilla, V. Caliva, M.C. D'Antonio, A.C. González-Baró, E.J. Baran, Vibrational spectroscopic investigation of the hydrates of manganese(II) oxalate, J. Raman Spectrosc. 40 (2009) 915–920, https://doi.org/10.1002/jrs.2200.
[51] M.G. Lioliou, C.A. Paraskeva, P.G. Koutsoukos, A.C. Payatakes, Heterogeneous nucleation and growth of calcium carbonate on calcite and quartz, J. Colloid Interface Sci. 308 (2007) 421–428, https://doi.org/10.1016/J.JCIS.2006.12.045.
[52] Y.-P. Lin, P.C. Singer, Effects of seed material and solution composition on calcite precipitation, Geochim. Cosmochim. Acta 69 (2005) 4495–4504, https://doi.org/10.1016/J.GCA.2005.06.002.
[53] M. Augustin, D. Fenske, I. Bardenhagen, A. Westphal, M. Knipper, T. Plaggenborg, J. Kolny-Olesiak, J. Parisi, Manganese oxide phases and morphologies: a study on calcination temperature and atmospheric dependence, Beilstein J. Nanotechnol. 6 (2015) 47–59, https://doi.org/10.3762/bjnano.6.6.